



# Hyper-selective plasmonic color filters

DAGNY FLEISCHMAN,<sup>1</sup> LUKE A. SWEATLOCK,<sup>1,2</sup> HIROTAKA MURAKAMI,<sup>3</sup>  
AND HARRY ATWATER<sup>1,\*</sup>

<sup>1</sup>California Institute of Technology, 1200 E California Blvd, Pasadena, CA 91125, USA

<sup>2</sup>Northrop Grumman NG Next, One Space Park, Redondo Beach, CA 90250, USA

<sup>3</sup>Sony Semiconductor Solutions Corporation, 4-14-1 Asahi-cho, Atsugi-shi, Kanagawa, 243-0014, Japan

\*[haa@caltech.edu](mailto:haa@caltech.edu)

**Abstract:** The subwavelength mode volumes of plasmonic filters are well matched to the small size of state-of-the-art active pixels in CMOS image sensor arrays used in portable electronic devices. Typical plasmonic filters exhibit broad ( $> 100$  nm) transmission bandwidths suitable for RGB or CMYK color filtering. Dramatically reducing the peak width of filter transmission spectra would allow for the realization of CMOS image sensors with multi- and hyperspectral imaging capabilities. We find that the design of 5 layer metal-insulator-metal-insulator-metal structures gives rise to multi-mode interference phenomena that suppress spurious transmission features and give rise to single transmission bands as narrow as 17 nm. The transmission peaks of these multilayer slot-mode plasmonic filters (MSPFs) can be systematically varied throughout the visible and near infrared spectrum, leading to a filter that is CMOS integrable, since the same basic MSPF structure can operate over a large range of wavelengths. We find that MSPF filter designs that can achieve a bandwidth less than 30 nm across the visible and demonstrate experimental prototypes with a FWHM of 70 nm, and we describe how experimental structure can be made to approach the limits suggested by the model.

© 2017 Optical Society of America

**OCIS codes:** (250.5403) Plasmonics; (050.6624) Subwavelength structures.

## References and links

1. M. Khoso and K. Kamra, "Smartphones: A Supercomputer in Your Pocket," <http://www.northeastern.edu/levelblog/2016/04/21/smartphones-supercomputer-in-your-pocket/>.
2. "Sensors Overview," [https://developer.android.com/guide/topics/sensors/sensors\\_overview.html](https://developer.android.com/guide/topics/sensors/sensors_overview.html).
3. S. Yokogawa, S. P. Burgos, and H. A. Atwater, "Plasmonic color filters for CMOS image sensor applications," *Nano Lett.* **12**(8), 4349–4354 (2012).
4. S. P. Burgos, S. Yokogawa, and H. A. Atwater, "Color imaging via nearest neighbor hole coupling in plasmonic color filters integrated onto a complementary metal-oxide semiconductor image sensor," *ACS Nano* **7**(11), 10038–10047 (2013).
5. T. Xu, Y.-K. Wu, X. Luo, and L. J. Guo, "Plasmonic nanoresonators for high-resolution colour filtering and spectral imaging," *Nat. Commun.* **1**, 59 (2010).
6. B. Y. Zheng, Y. Wang, P. Nordlander, and N. J. Halas, "Color-selective and CMOS-compatible photodetection based on aluminum plasmonics," *Adv. Mater.* **26**(36), 6318–6323 (2014).
7. T. W. Ebbesen, H. J. Lezec, H. F. Ghaemi, T. Thio, P. A. Wolff, T. Thio, and P. A. Wolff, "Extraordinary optical transmission through sub-wavelength hole arrays," *Nature* **391**, 694–697 (1998).
8. J. A. Dionne, L. A. Sweatlock, H. A. Atwater, and A. Polman, "Plasmon slot waveguides: Towards chip-scale propagation with subwavelength-scale localization," *Phys. Rev. B* **73**, 03547 (2006).
9. Q. Chen, X. Hu, L. Wen, Y. Yu, and D. R. S. Cumming, "Nanophotonic Image Sensors," *Small* **12**(36), 4922–4935 (2016).
10. H. Wang, X. Wang, C. Yan, H. Zhao, J. Zhang, C. Santschi, and O. J. F. Martin, "Full Color Generation Using Silver Tandem Nanodisks," *ACS Nano* **11**(5), 4419–4427 (2017).
11. A. Kristensen, J. K. W. Yang, S. I. Bozhevolnyi, S. Link, P. Nordlander, N. J. Halas, and N. A. Mortensen, "Plasmonic colour generation," *Nat. Rev. Mater.* **2**, 16088 (2016).
12. L. Frey, P. Parrein, J. Raby, C. Pellé, D. Héault, M. Marty, and J. Michailos, "Color filters including infrared cut-off integrated on CMOS image sensor," *Opt. Express* **19**(14), 13073–13080 (2011).
13. T. Hirayama, "CMOS Image Sensor Evolution: Past, Present, and Future," in *SEMICON Europa* (2016).
14. W.-Y. Jang, Z. Ku, J. Jeon, J. O. Kim, S. J. Lee, J. Park, M. J. Noyola, and A. Urbas, "Experimental Demonstration of Adaptive Infrared Multispectral Imaging using Plasmonic Filter Array," *Sci. Rep.* **6**, 34876 (2016).

15. A. A. Gowen, C. P. O'Donnell, P. J. Cullen, G. Downey, and J. M. Frias, "Hyperspectral imaging – an emerging process analytical tool for food quality and safety control," *Trends Food Sci. Technol.* **18**, 590–598 (2007).
16. E. K. Hege, D. O'Connell, W. Johnson, S. Basty, and E. L. Dereniak, "Hyperspectral imaging for astronomy and space surveillance," *Opt. Sci. Technol. SPIE's 48th Annu. Meet.* **5159**, 380–391 (2004).
17. S. S. Wang and R. Magnusson, "Theory and applications of guided-mode resonance filters," *Appl. Opt.* **32**(14), 2606–2613 (1993).
18. D. B. Mazulquim, K. J. Lee, J. W. Yoon, L. V. Muniz, B.-H. V. Borges, L. G. Neto, and R. Magnusson, "Efficient band-pass color filters enabled by resonant modes and plasmons near the Rayleigh anomaly," *Opt. Express* **22**(25), 30843–30851 (2014).
19. Z. Li, S. Butun, and K. Aydin, "Large-area, Lithography-free super absorbers and color filters at visible frequencies using ultrathin metallic films," *ACS Photonics* **2**, 183–188 (2015).
20. H. Gao, W. Zhou, and T. W. Odom, "Plasmonic crystals: A platform to catalog resonances from ultraviolet to near-infrared wavelengths in a plasmonic library," *Adv. Funct. Mater.* **20**, 529–539 (2010).
21. D. Pacifici, H. J. Lezec, L. A. Sweatlock, R. J. Walters, and H. A. Atwater, "Universal optical transmission features in periodic and quasiperiodic hole arrays," *Opt. Express* **16**(12), 9222–9238 (2008).
22. A. Mazor, D. J. Srolovitz, P. S. Hagan, and B. Bukiet, "Columnar growth in thin films," *Phys. Rev. Lett.* **60**(5), 424–427 (1988).
23. A. A. Maradudin and D. L. Mills, "Scattering and absorption of electromagnetic radiation by a semi-infinite medium in the presence of surface roughness," *Phys. Rev. B* **11**, 1392–1415 (1975).
24. O. J. Martin, K. Thyagarajan, and C. Santschi, "A New Fabrication Method for Aluminum and Silver Plasmonic Nanostructures," in *Workshop on Optical Plasmonic Materials* (The Optical Society of America, 2014).
25. A. Joshi-Imre and S. Bauerdick, "Direct-Write ion beam lithography," *J. Nanotechnol.* **2014**, 170415 (2014).

## 1. Introduction

Today's state-of-the-art mobile electronics are as powerful as larger computers [1], and are equipped with a variety of sensors including accelerometers, gyroscopes, CMOS image sensors, and magnetometers [2]. CMOS image sensors have a particularly broad landscape of potential new functions: optical data on mobile platforms today consists primarily of three-color imaging, but a wide variety of applications could be accessed by the collection of high resolution spectroscopic information. Plasmonic structures have been demonstrated as a color filter platform well-suited for CMOS integration due to the small mode volumes of plasmons and the CMOS compatibility of many of the materials that support them. Plasmonic hole and slit array color filters have been demonstrated as a viable alternative to dye-based filters for RGB and CMYK color-filtering [3–8]. In addition to hole and slit array filters, many other geometries have been explored as potential platforms for commercially viable plasmonic color filters [9–12]. Recently, this spate of development has been translated into industrial CMOS image sensor prototypes and are actively being considered for full commercialization [13].

Previous work has demonstrated plasmonic hole and slit array color filters capable of filtering the visible spectrum into three or four broad spectral bands ( $>100$  nm) [3–8]. By reducing the transmission bandwidth of the filters to less than 30 nm, CMOS image sensors would gain the ability to perform multi- and hyper-spectral imaging without needing to rely on algorithmic post-processing [9,14]. Multi- and hyper-spectral imaging is utilized in a wide range of terrestrial and space applications, and providing portal devices with this functionality would have implications spanning food quality control to space exploration [15,16]. Guided mode resonance filters have been shown capable of generating high intensity, narrowband filtering [17]. However, the millimeter-scale of these filters is impractical for CMOS integration [18]. Narrow bandwidth responses have also been reported in thin filmed multi-layer plasmonic structures [19]. The peak wavelength of these structures is tuned via changing the thickness of the intermediate dielectric layer, so the many lithographic steps needed to patterns the tens to hundreds of spectral bands make these structures infeasible for multi- and hyper-spectral filtering. In this work, we have designed and prototyped a micron-scale plasmonic color filter capable of narrow band-pass transmission ( $<30$  nm). The filters span the visible and near infrared spectrum and all utilize the same planar stack of materials where the peak transmission wavelength is determined through a single lithographic step.

Plasmonic color filters utilizing periodic arrays of subwavelength holes or nanoslits in metal films enable efficient conversion of optical energy between incident photons and surface propagating two-dimensional charge density waves, surface plasmon polaritons (SPPs). Due to the permittivity discontinuity at metal-dielectric surfaces, SPPs have an in-plane momentum  $k_{\text{SPP}}$  greater than that of light in free space  $k_0$ . Patterned metal surfaces including gratings, or arrays of holes or slits, allow the matching of momentum and thereby enable efficient conversion of light into SPPs via scattering. The strength of interaction between photons and SPPs can be tailored by changing geometric factors such as the shape of the scattering elements, and the symmetry and periodicity of the array as well as by selecting the permittivity of the constituent materials [20].

In particular, periodic arrays of subwavelength apertures passing through a metal film exhibit enhanced transmission exclusively at conditions corresponding to constructive mutual interference between incident light and SPPs traveling along the surface between adjacent slits. In the case that the metallic layer is thick enough to be substantially opaque to incident photons, the SPP mediated process is the dominant mode of transmission and the surface acts as a band-pass color transmission filter. Such aperture arrays have been the topic of substantial scientific interest due to these remarkable optical properties and their utility as a testbed for studying fundamental light-matter interactions in plasmonic systems [7,21].

The dispersion of plasmonic propagating modes can be further engineered using metal-clad slot waveguides, often realized as multilayer stacks with a metal-insulator-metal (MIM) configuration [8]. Such MIM stacks may support a multitude of polaritonic modes which lie either inside or outside the “light cone,” that is, with in-plane momentum either greater or less than that of a photon with equal energy. This additional degree of freedom enables substantially more complex optical transmission filter spectra enabling narrow bandwidth suitable for multi- and hyperspectral color filtering applications [5].

## 2. Designing plasmonic color filters

Finite difference time domain methods (FDTD) were used to determine the transmission spectra of different filter structures. Figure 1 illustrates the different types of transmission filters and their spectral behavior. MIM have been used to make RGB color filters [5]. These structures can be optimized to have narrowband transmission, but as the structure is optimized to minimize FWHM of the transmission peak, the intensity of the next highest order mode increases. This trade-off can be lifted by introducing a second MIM mode into the structure that couples with the original MIM mode, leading to the suppression of the spurious transmission. The multilayer slot-mode plasmonic filter (MSPF) investigated demonstrates a narrow transmission bandwidth and spurious peak suppression, as shown in Fig. 1(b), and by changing the periodicity of the slits, this filter can be swept across the entire visible spectrum.

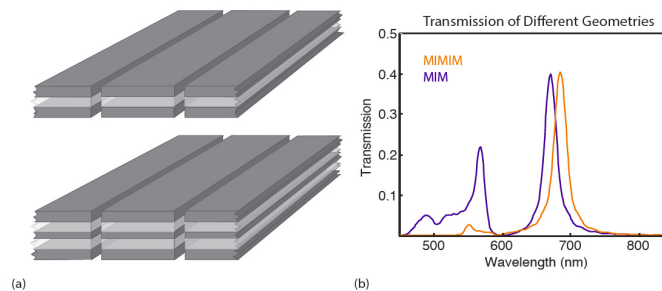


Fig. 1. (a) Schematics of MIM and MIMIM filter structures. All dark grey metal layers are Ag and 70 nm thick, except for the 50 nm center metal layer of the MIMIM filter. All light grey insulating layers are 70 nm of SiO<sub>2</sub> (b) Comparison between MIM and MIMIM transmission behavior shows similar FWHM but enhanced suppression of the secondary peak in the MIMIM case.

The MSPFs were optimized using an incident TM plane wave source. Optimizations were conducted via a series of parameter sweeps that considered both the thicknesses and optical indices of all the insulating and metallic layers, as well as the width and spacing of the milled slits. The initial values for the thicknesses of the metallic layers were determined by considering the skin and penetration depths of various metals. For a successful filter, the top and bottom metallic layers of the structure must be sufficiently thick to be opaque across the visible and near IR parts of the electromagnetic spectrum. Using data from Rakic et al. for Ag as an example, the  $1/e$  penetration depth ( $d_p$ ) of Ag was calculated to range from 12.9 nm – 16.8 nm across the visible spectrum. To prevent 98% of light from penetrating the structure, the top and bottom layers must be at least 4 times  $d_p$ . Therefore 68 nm was used as the initial parameter sweep value when optimizing the system that utilized Ag.

Likewise, the starting point for the thickness of the insulating layers was approximated by considering the propagating modes guided laterally within the structure. Numerically determined dispersion curves derived from experimental optical constants of Ag and SiO<sub>2</sub> can be used to determine the available modes within an MIM [8]. For SiO<sub>2</sub> thicknesses of less than 100 nm, traditional photonic waveguide modes are cut off in an Ag/SiO<sub>2</sub>/Ag system, so the waveguide only supports high-momentum surface plasmon modes. Therefore, the parameter sweeps used 100 nm as the upper value restriction for the SiO<sub>2</sub> thickness of each waveguide.

Iterating over the parameter sweep led to the final device structure, with alternating layers of Ag and SiO<sub>2</sub>. Both SiO<sub>2</sub> layers were optimized to 70 nm, the top and bottom Ag layers are 70 nm and the spacer layer is 50 nm. The width of the slit is 50 nm for all filters and the slit periodicities investigated vary from 250 nm to 550.

The position of the transmission peak varies linearly with the periodicity of the slits and, as shown in Fig. 2(a), peak position can be swept across the visible and near IR spectrum. Therefore, just by varying the inter-slit pitch, a series of MSPFs with the same layer materials and thicknesses can be used as a color filter across a wide range of the spectrum. The FWHM of the transmission spectra are about 20 nm on average with no peak exceeding 28 nm, as shown in Fig. 2(b). Additionally, the overall transmission of the side-lobe peak does not exceed 11% of that of the primary peak in the visible portion of the spectrum, and does not exceed 25% of the primary peak intensity in all filters investigated. While it is possible to design MSPF filters using other materials systems, the Ag/SiO<sub>2</sub> system was found to be most optimal. For example, the transmission spectrum of an optimized Al/SiO<sub>2</sub> MSPF possesses a FWHM of 34 nm and peak transmission of just over 20%.

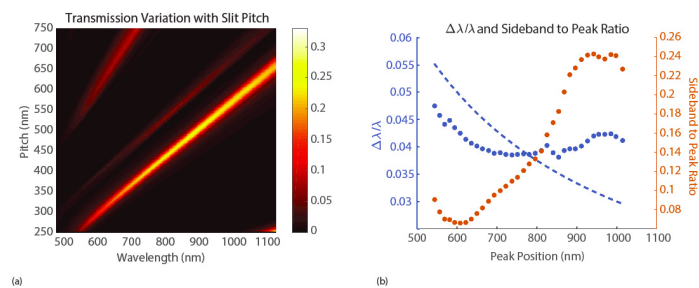


Fig. 2. (a) Superposition of the transmission behavior of filters with varying slit pitches. As slit pitch increases the narrowband transmission peak is controllably shifted to longer wavelengths (b) The relationship between FWHM, peak position, and sideband to peak ratio. The blue axis illustrates the ratio of FWHM to the peak position. The dashed line sets the threshold of a 30nm FWHM, and the dotted line illustrates the ratio of the transmission peak's FWHM to the peak position. The dotted line is beneath the dashed line for the entire visible spectrum, indicating that all filters fulfill the criteria for hyperspectral imaging. The orange dotted line illustrates the ratio between the sideband and main intensity peaks, showing the best filters are also in the visible part of the spectrum.

### 3. Experimental verification

MSPFs were fabricated by depositing alternating layers of Ag and SiO<sub>2</sub> in an electron beam evaporator onto a solvent cleaned fused silica slide and then subsequently milled using a focused ion beam (FIB). The 50 nm slit milled into a 330 nm structure is a prohibitively demanding aspect ratio for a FIB trench mill. For a set of proof-of-concept filters, these demanding design conditions can be relaxed by considering filters only towards the lower energy portion of the visible spectrum. For a slit width of 120 nm, the suppression of the spurious transmission peak is retained and the FWHM of the primary transmission peak only takes a 25 nm hit.

When Ag is deposited on SiO<sub>2</sub> in an electron beam evaporator, the Ag films grow with a columnar growth mechanism [22]. These films are rough, which increases plasmonic loss, thereby reducing overall transmission intensity of the filter [23]. The roughness of Ag deposited on SiO<sub>2</sub> is even more problematic in a multilayer structure like the MSPF because the roughness of each Ag layer compounds. A rough substrate increases the roughness of the film deposited on it due to differences in atomic flux received by areas of the film with positive and negative curvatures that are larger than can be compensated for by surface diffusion [22]. Because the SiO<sub>2</sub> conformally deposits on the underlying Ag layer, each Ag layer sees a progressively rougher substrate, leading to a very rough top surface of the MSPF.

By utilizing a seed layer of AgO deposited onto each SiO<sub>2</sub> surface, a much smoother Ag film can be deposited [24]. The AgO is deposited by slowly electron beam evaporating Ag at a rate of 0.1 A/s in a chamber with an O<sub>2</sub> pressure of  $9.5 \times 10^{-5}$  torr. Once 2 nm of AgO are on the surface of the SiO<sub>2</sub>, the deposition is paused and the AgO is held under vacuum for 10 minutes. Because AgO is not vacuum stable, the oxygen is pumped out of the film, leaving a thin Ag layer on the surface of the SiO<sub>2</sub> [24]. The deposition is then resumed and the rest of the Ag layer is deposited at in a chamber with pressure  $2.3 \times 10^{-6}$  torr and no oxygen flow. The roughness of Ag films deposited with this method was measured to have an RMS of 2.56 nm and the top Ag surface of a multilayer deposited with the AgO growth method has an RMS of 2.92 nm. Each Ag layer was deposited using this method.

To further protect the integrity of the filter, a sacrificial layer was put on the top Ag surface. First a 90 nm layer of 950 A2 PMMA was then spun onto the top surface of the MSPF and then another 70 nm layer of Ag was deposited on top of the PMMA. The sacrificial layer protects the top Ag film of the MSPF by confining the worst of the ion beam damage to the surface of the sacrificial layer, rather than the surface of the MSPF. To utilize the best possible resolution of the ion beam, the 130 nm wide slits are milled in FEI Versa FIB, at 30 kV and 1.5 pA [25]. The high accelerating voltage and low beam current help compensate for the high aspect ratio of the filter structure. Multi-pass milling is used to reduce the taper of the slits—first a rectangle is milled, followed by a frame around the perimeter to better define the edges and clean off reposition within the slit. The sacrificial layer is then removed using a heated solvent bath.

The fabricated filters are then measured using a supercontinuum laser with monochromator set-up that allows for the sample to be illuminated with a narrow bandwidth of incident radiation. A 5X objective takes the collimated light and focuses it down to a 10  $\mu\text{m}$  spot size with a 5.7° angular spread from the incident normal. The incident beam is shined on the 30  $\mu\text{m}$  x 30  $\mu\text{m}$  MSPFs. Squares equal in size to the filters were milled 100  $\mu\text{m}$  away from each filter and are used to determine the intensity of the laser. All transmitted power was collected by a Si photodiode that was affixed behind the substrate in which the filters and normalization squares have been milled. The experimental response of each filter was determined by normalizing the light transmitted through the filter by that transmitted through its corresponding normalization square.

Figure 3(a) shows the experimental transmission response of a prototype filter that has an inter-slit pitch of 475 nm. A cross section of the prototype filter was milled using the FIB.



The micrograph of the filter's cross-section, shown in Fig. 3(c) reveals that there is a slight taper to the filter structure. Using FDTD simulations, we can compute the transmission behavior of filters with a progressively increasing sidewall taper. The results of these simulations, shown in Fig. 3(b) illustrate the importance of the slit sidewalls on the overall behavior of the structure. Using the information gathered from the FDTD simulations, it was determined that to maintain filtering behavior with side lobe suppression, the sidewalls of the slit could not possess greater than a  $5^\circ$  taper. The side lobe in the experimental transmission is due in part to the  $13.7^\circ$  taper in the fabricated filter. In future work, this taper can be eliminated by utilizing nanoimprint lithography couple with advanced thin film deposition techniques to produce MSPF filters with less taper. Additionally, diffractively coupled resonances are angle sensitive, so the angular spread of the incident beam also led to slight broadening and side lobe enhancement.

The polarization response was also experimentally confirmed to match the simulated predications, as shown in Figs. 4(a) and 4(b). While the fabricated filters were polarization sensitive, Figs. 4(c) and 4(d) illustrate that the polarization dependence of MSPFs can be eliminated entirely by introducing a second array of slits perpendicular to the original slit array, allowing any incident k-vector to effectively couple into the plasmon modes of the filter.

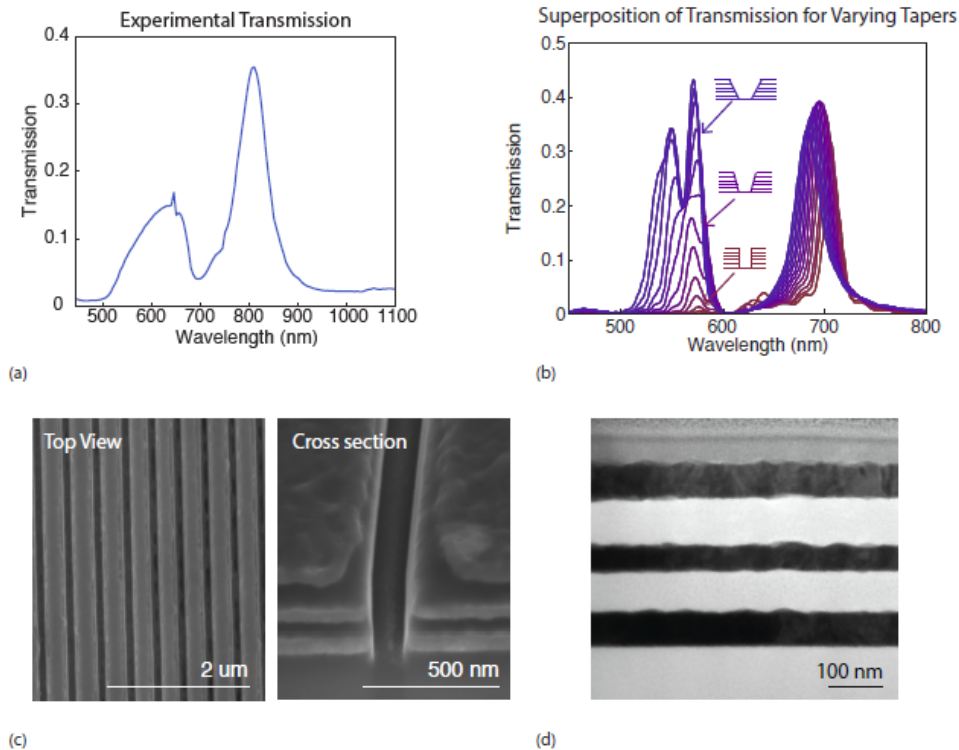


Fig. 3. (a) Experimentally determined transmission of a single MIMIM filter (b) Simulated dependence of transmission on taper of slits (c) Top down and cross-sectional SEMs of the MSPF filter (d) TEM micrograph showing the layer thicknesses and roughness of the five layers of the filter.

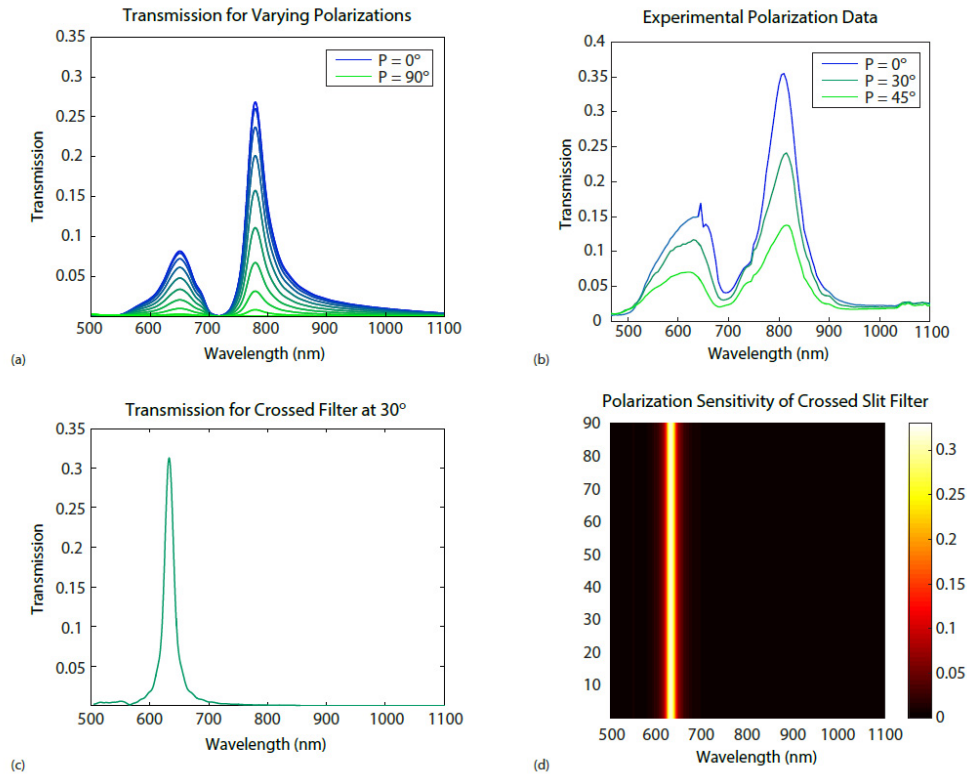


Fig. 4. (a) Simulated polarization response varying from  $0^\circ$  (blue) to  $90^\circ$  (green) (b) The simulated polarization response was confirmed experimentally, with a  $0^\circ$  measurement (blue), a  $30^\circ$  measurement (teal), and a  $45^\circ$  measurement (green) (c) A transmission spectrum for a crossed MSPF structure with incident polarization oriented at  $30^\circ$  from the original grating normal (d) Superposition of transmission curves spanning  $0^\circ$  to  $90^\circ$  for a crossed MSPF structure showing complete polarization insensitivity.

#### 4. Analytical analysis

A series of FDTD simulations was performed in order to study the electromagnetic modes that propagate in the MIMIM device stack. To study fundamental properties of these guided mods, light is coupled into the stack using plane wave illumination of a single slit, as opposed to the periodic array of slits that comprise the MSPF structures. A series of 211 single frequency TM plane wave excitations were used to sweep over the entire visible spectrum. Complex vector field data was collected by finely meshed monitors capturing the EM time evolution of each of the FDTD simulations. This data set can be compressed by taking a discrete-time Fourier transform at runtime which transforms the time-harmonic field data in the frequency domain.

In Fig. 5(a), a single electric field component is plotted from the compressed data set of a sample simulation conducted at an excitation energy of 1.88 eV. The spatial mapping of the electric field depicts light scattered by a slit at  $z = 0$  into multiple modes propagating in the  $z$ -direction. These modes have high field intensity within both  $\text{SiO}_2$  layers as well as the top and bottom Ag surfaces. The spatial mapping of the electric field indicates that slit preferentially couples energy into the topmost  $\text{SiO}_2$  layer. Coupling between the two dielectric layers is also apparent, as a characteristic beating pattern is observed indicating that power is oscillating between the two MIMs. This result was expected physically—the spacer layer between the two insulating layers is thinner than the skin depth of Ag at this photon energy.

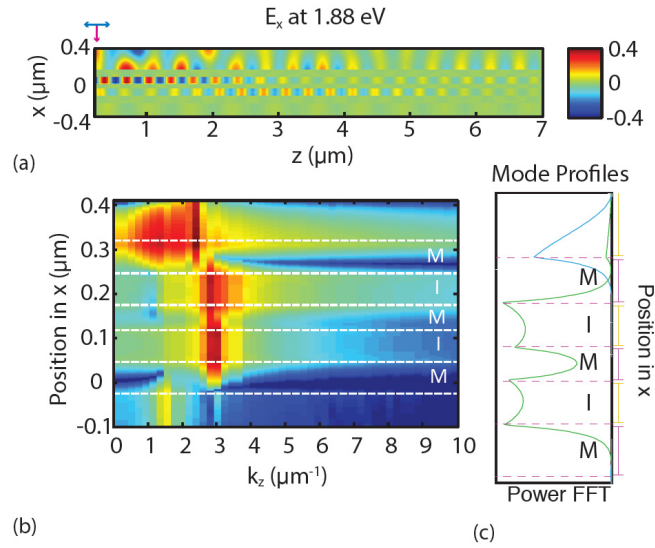


Fig. 5. (a) Fields resulting after a TM plane wave, incident in the negative  $x$  direction, scatters at a single slit and couples into MIM modes propagating in the  $z$  direction (b) An FFT of the fields at a single excitation frequency shows multiple modes resolved by wavenumber (c) Cross section through the FFT data at a select wavenumber reveals the spatial mode profile.

To better determine the natures of the various modes within the MSPF, a second Fourier Transform was performed. Using Eq. (1), an FFT was taken over the propagation direction of the modes ( $z$ ), thereby moving the phasor direct space data set into momentum space (i.e. “ $k$ -space”).

$$f(k) = \int F(z)e^{-ikz} dz \quad (1)$$

The results of this FFT can be plotted, as shown in Fig. 5(b), to illustrate the various modes excited by the single frequency source. The vertical streaks in the spectral power map indicate there are modes at multiple propagation wavevectors ( $k_z$ ) at this excitation frequency. Vertical cross-sections through this data set describe the spatial field profile along the  $x$ -axis transverse to the propagation direction, and can provide insight into the nature of particular modes. For example, the dark red streak at  $k_z = 2.7 \mu\text{m}^{-1}$  is localized on the metallic surface of the MSPF filter, and therefore this feature can be identified as an SPP. Indeed, this corresponds to the expected wavenumber for an SPP on the surface of an Ag film at this excitation frequency.

Close inspection of the intensity patterns of the hot spots in Fig. 5(b) reveals that the region of high spectral power on the surface of the filter at wavenumbers less than  $2.7 \mu\text{m}^{-1}$  corresponds to unbound modes that do not contribute to filter behavior. After discarding the evanescently reflecting quasi-modes, the nature of the remaining modes can be determined by plotting the linear intensity variations at each wavenumber that possesses a streak of high spectral power, superimposing these linear intensity variations on the same axis yields the plot shown in Fig. 5(c). This plot depicts the two strongest plasmon modes in the structure: the mode on the top surface of the filter and the mode spanning the insulating layers contained within the filter. The predominant surface mode, shown in blue in Fig. 5(c), corresponds to SPPs excited at the top Ag surface of the filter. The other excitation is a super-mode corresponding to a coupling of the two MIM modes generated within each of the two insulating layers in the structure. This is the mode that was implied in the spatial field map in Fig. 5(a) is now clearly depicted in Fig. 5(c), which reveals that the two MIM modes within the super-mode are coupled because of strong field overlap within the 50 nm Ag spacer.



The behavior of the energy propagating through the filter can be determined by the FFT analysis, but it does not indicate how these modes contribute to the overall behavior of the filter. The contribution of each mode to the unsuppressed transmission peak can be determined by normalizing the transmission curves of the periodic grating MSPF structures over the dispersion curve of each mode and the pitches of the filter gratings.

The dispersion curve of each plasmon mode can be determined by constructing a dispersion curve for the MSPF. The dispersion curve shown in Fig. 6(a) was constructed by using the Fourier Transformed k-space data sets and plotting the power of the modes at each spectral frequency as a function of energy. The two branches on curve correspond to the bottom side SPP and the metal-insulator-metal-insulator-metal (MIMIM) super-mode, and can be mapped to the frequency values that correspond to these modes in Fig. 5(c). The lower intensity signal plotted to the left of the branches corresponds to the unbound quasi-modes bouncing off the surface of the filter. From the data contained within this plot, the dispersion curve for each of the two modes can be analytically determined.

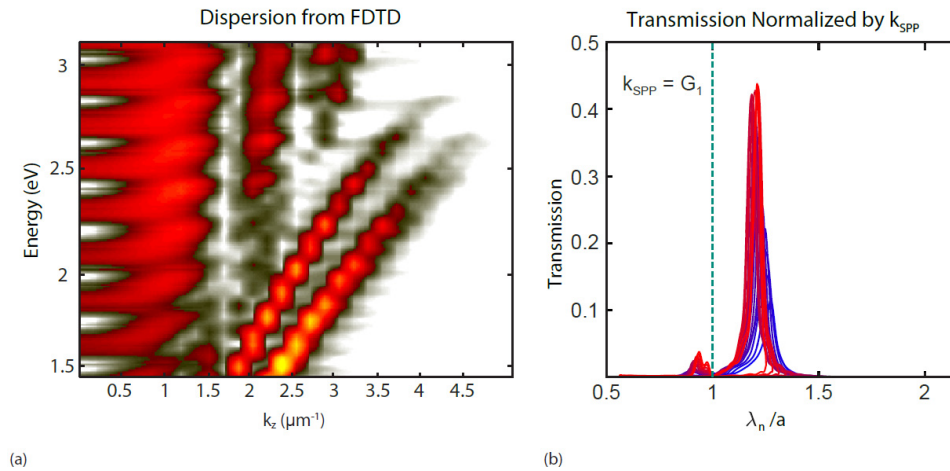


Fig. 6. (a) By taking FFTs of a sweep of single frequency excitations, a dispersion curve can be constructed that illustrates the behavior of both active modes (b) Universal curve analysis confirms that the SPP mode on the top surface of the MSPF filter is predominantly responsible for the filters transmission behavior. The various colors of the transmission curves correspond to different peak intensity positions that have all been normalized by the SPP dispersion curve.  $G_1$  is the lowest order reciprocal lattice vector and a corresponds to the pitch of the slits.

The transmission behavior was first normalized over the pitch of the filter grating to lift the dependence of the transmission curves on that characteristic of the filters [21]. Figure 6(b) shows the transmission curves normalized by the SPP dispersion curve, leading to curves aligned between 0.5 and 1, with the transmission minima collapsing at 1 on the normalized axis [21]. This behavior illustrates that the SPP mode satisfies the momentum matching condition required for it to contribute to the transmission behavior of the filter, with the MIMIM super-mode acting as a supplementary suppression to remove the second highest order peak. This analysis confirms the origin of the spurious peak in the experimental results. As the slits are tapered, the difference between the lengths of the two channels increases, which affects the interference between the two modes. The change in interference behavior reduces the filtering efficiency of this mode and allows multiple orders of modes to propagate through the structure, leading to a reduced suppression of the spurious peak.

## 5. Conclusions

A plasmonic color filter with a single narrowband transmission response was designed using FDTD and fabricated to confirm the simulated response. The filter is readily amenable to device integration, with a size well-matched to state of the art CMOS image sensors. The plasmonic filter utilizes a geometry that flexibly allows for precise selection of the spectral bands of interest, allowing for portable electronic devices to be capable of multi- and hyperspectral imaging. The behavior of this filter was analytically determined to arise from a combination of SPP excitations—the surface SPP mode leads to the enhanced transmission behavior associated with subwavelength plasmonic filters, while the slightly asymmetric MIM super-mode leads to the suppression of the spurious transmission peak that arises in other narrowband plasmonic filter geometries. The MSPF is inherently gated, and this feature will be capitalized on in future work by incorporating transparent conducting oxides into this geometry to create tunable narrowband color filters spanning both the visible and near infrared parts of the spectrum.

## Funding

Sony Corporation; the Hybrid Nanophotonics Multidisciplinary University Research Initiative Grant (Air Force Office of Scientific Research FA9550-12-1-0024); Northrop Grumman Corporation.

## Acknowledgments

LAS acknowledges support from the Resnick Sustainability Institute at Caltech. DF gratefully acknowledges helpful discussions with Michelle Sherrott, Max Jones, Matt Sullivan, and Charles Shaw. The facilities of the Kavli Nanoscience Institute (KNI) at Caltech are gratefully acknowledged.